Letter

# Unveiling Mn$^{2+}$ Dopant States in Two-Dimensional Halide Perovskite toward Highly Efficient Photoluminescence

Binbin Su, Maxim S. Molokeev, and Zhiguo Xia*

ACCESS | Metrics & More | Article Recommendations | SI Supporting Information

**ABSTRACT:** Doping is able to create novel optoelectronic properties of halide perovskites, and the involved mechanism of efficient emission is still a challenge. Herein Mn$^{2+}$ substitution into 2D layered perovskites $(C_8H_{20}N_2)PbBr_4$ was investigated, demonstrating broad-band orange-red emission originating from the $^4T_1 \rightarrow ^6A_1$ transition of Mn$^{2+}$ dopant. The photoluminescence quantum yield (PLQY) of Mn$^{2+}$ emission is up to 60.8% related to the energy transfer in coupled states. We verify that an actual Mn$^{2+}$ dopant as low as 0.476% reaches a high PLQY, whereas the nominal adding amount is 0.8 as the Mn$^{2+}$/Pb$^{2+}$ ratio. The small activation energy (∼6.72 meV) between the Mn$^{2+}$ d state and the trap state accounts for this highly efficient energy transfer and photoluminescence. The proposed luminescence mechanism in Mn$^{2+}$-doped 2D halide perovskites would provide unique insights into the doping design toward high-performance luminescence materials.
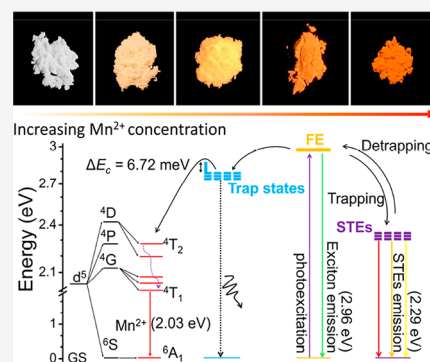
Organic−inorganic halide perovskites are currently receiving plenty of attention owing to their attractive physical properties and potential for optoelectronics devices.[1,2] Rational doping can provide a unique path to endow them with additional optical properties and unexpected functionalities in targeted compounds.[3,4] To date, the substitution of different metal ions into halide perovskites, such as Na$^+$, Cu$^{2+}$, Mn$^{2+}$, Cd$^{2+}$, Sr$^{2+}$, Zn$^{2+}$, or rare earth ions for the Pb$^{2+}$ cation has been realized to tailor their properties.[5−10] In particular, doping of the Mn$^{2+}$ cation not only generates new optical properties but also endows original materials with additional properties, including improved physical and chemical stabilities, enhanced photoluminescence quantum yields (PLQYs), passivated grain boundaries, and reduced defect state densities.[11,12] Moreover, the optoelectronics devices constructed with doped perovskites exhibit prominent performance.[9,13−15] As a result, the doping of Mn$^{2+}$ into multifarious halide perovskites has been widely studied, including 0D, 2D, 3D, and double perovskites.[16−20]

It is of interest to note that Mn$^{2+}$-doped 2D halide perovskites have potential for light-emitting diode applications due to their enhanced chemical stability and characteristic strongly bound exciton, which benefit an increase in the dopant−carrier exchange interactions for efficient energy transfer.[21−26] Kundu et al. first reported Mn$^{2+}$-doped 2D layered perovskites $(C_4H_9NH_3)_2PbBr_4$ by simple mechanical grinding and thermal annealing, and the materials demonstrated enhanced the energy transfer efficiency from the strongly bound excitons to the Mn$^{2+}$ d states, leading to the broad-band Mn$^{2+}$ emission with the highest PLQY of 37%.[18] They also found significant energy transfer between host microparticles and Mn$^{2+}$ that results in Mn$^{2+}$ emission with a PLQY of 36%.[27] However, most reported Mn$^{2+}$-doped 2D

layered perovskites have relatively low PLQYs within the range of 10−40%, except for several limited individuals.[28−33] It must be pointed out that the PLQYs of doped halide perovskites were related to many factors, such as structure types, particle sizes, compositions, ligand types, and so on.[20,32,34,35] As an example, our group recently investigated the effect of halogen compositions on the photoluminescence of Mn$^{2+}$-doped $BA_2PbX_4$ (BA = $C_4H_9NH_3$, X = Cl, Br, I) 2D perovskites, which has provided new insight into the chemical mechanism of Mn$^{2+}$ doping on the emission.[36] In addition to the facts previously mentioned, the involved energy transfer mechanism from the host to dopants is also important for effecting the PLQYs of doped perovskites. However, the energy transfer mechanism related to Mn$^{2+}$ dopant amounts and different coupled states in 2D hybrid perovskites has rarely been studied, and thus it is essential to investigate the dopant emission, especially the energy transfer mechanism in Mn$^{2+}$-doped 2D halide perovskites.

Here 2D halide perovskite $(C_8H_{20}N_2)PbBr_4$ was designed and demonstrated broad-band emission with a PLQY of 6.6%, comprising a narrow free exciton (FE) peak located at 418 nm and a broad-band self-trap exciton (STE) emission from 450 to 750 nm, centered at 540 nm. More importantly, Mn$^{2+}$-doped $(C_8H_{20}N_2)PbBr_4$ showed a strong orange-red emission peaking

at 610 nm originating from the $^4T_1 \rightarrow {}^6A_1$ transition of the $Mn^{2+}$ ion with the highest PLQY of up to 60.8%. It is found from the structure and chemical composition analysis that the actual $Mn^{2+}$ doping content is as low as 0.476%, and even the nominal adding amount reaches 0.8 as the ratio of $Mn^{2+}/Pb^{2+}$. The $Mn^{2+}$ emission is related to the efficient trapping of excitons by the defect level induced by dopants; moreover, the small activation energy (~6.72 meV) between the $Mn^{2+}$ d state and the trap state can also take effect. This work will provide new ideas on how tuning the doping state and the amount of $Mn^{2+}$ activators in the halide perovskites enables us to control the efficient energy transfer and photoluminescence.

The single-crystal products of $(C_8H_{20}N_2)PbBr_4$ were grown in a sealed stainless-steel Parr autoclave by the programmed temperature lowering method (see details in the Supporting Information (SI)). White single crystals of $(C_8H_{20}N_2)PbBr_4$ of relatively large size (~0.8 cm) were obtained, as shown in the photograph (Figure 1a). The crystal structure of $(C_8H_{20}N_2)$-
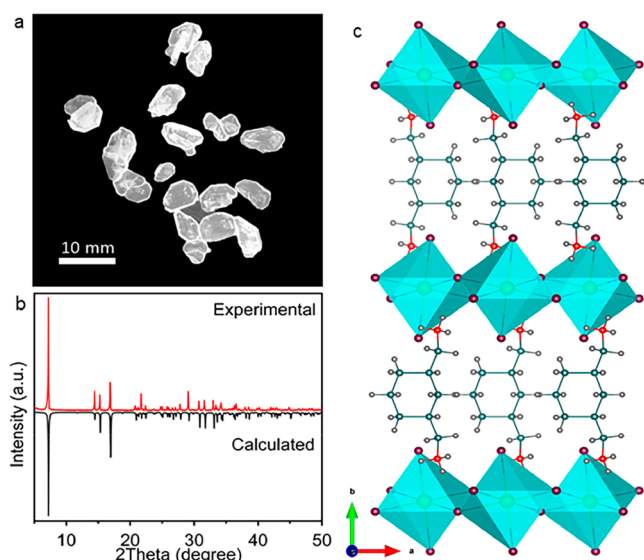


**Figure 1.** (a) Optical photograph of $(C_8H_{20}N_2)PbBr_4$ crystals under 365 nm UV irradiation. (b) Simulated and experimental powder X-ray diffraction pattern of $(C_8H_{20}N_2)PbBr_4$. (c) Crystal structure diagram of 2D layered $(C_8H_{20}N_2)PbBr_4$ (yellow, lead atoms; reddish brown, bromine atoms; red, nitrogen atoms; green, carbon atoms; gray, hydrogen atoms; blue polyhedron, $PbBr_6$ octahedron).

$PbBr_4$ was analyzed by the single-crystal X-ray diffraction (SCXRD) technique, revealing an orthorhombic structure with space group *Pnma*, which is consistent with a previous report.[37] The experimental powder X-ray diffraction (PXRD) patterns match fairly well with the calculated data based on the single-crystal structure of $(C_8H_{20}N_2)PbBr_4$ (Figure 1b). The crystallographic information file (CIF) of $(C_8H_{20}N_2)PbBr_4$ is given in the Supporting Information. The main crystallographic data, fractional atomic coordinates, and isotropic or equivalent isotropic displacement parameters are shown in Tables S1 and S2, respectively. $(C_8H_{20}N_2)PbBr_4$ appears as a typical layered 2D structure. As shown in Figure 1c, the $Pb^{2+}$ ion is coordinated by six $Br^-$ ions, which are connected to each other by nodes forming a 2D layer, to form a $PbBr_6$ octahedron. The Pb−Br distances lie in the range of 2.9710(34) to 3.0198(4) Å (Table S3). The $[PbBr_6]^{4-}$ octahedron propagates in the *ac* plane with channels along the *b* axis held by organic cations $[C_8H_{20}N_2]^{2+}$ (Figure 1c). In

general, the distortion degree of the inorganic part is determined by the $PbBr_6$ octahedron and the state between the adjacent $PbBr_6$ octahedrons. Herein the distortion parameter ($\Delta d$) is calculated based on the following equation

$$\Delta d = \left(\frac{1}{6}\right) \sum \left[\frac{d_n - d}{d}\right]^2 \tag{1}$$

where $d$ defines the average Pb−Br bond length and $d_n$ denotes the distances of six individual Pb−Br bonds. The average Pb−Br distance in $(C_8H_{20}N_2)PbBr_4$ is determined to be 3.0029 Å. Finally, $\Delta d$ is calculated to be $1.124 \times 10^{-4}$, indicating that the $PbBr_6$ octahedron is distorted. The calculated Pb−Br−Pb angle at 147.647° in the *ac* plane presents a large deviation because it strongly deviates from the planar geometry at the ideal 180° (Figure S1). Such structural character indicates that $(C_8H_{20}N_2)PbBr_4$ will have potential as a broad-band emitter.

$(C_8H_{20}N_2)PbBr_4$ powders were prepared according to the procedure described in the experimental section and possessed the same characteristics as the single-crystal counterparts. The absorption and emission spectra of the $(C_8H_{20}N_2)PbBr_4$ powder were measured and are demonstrated in Figure 2.
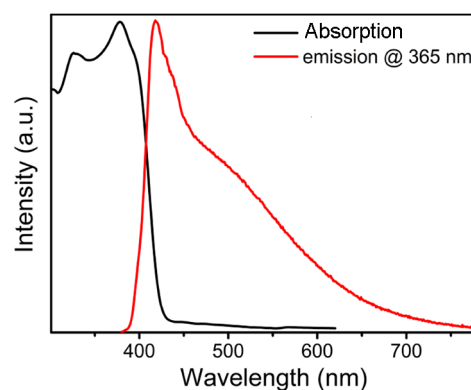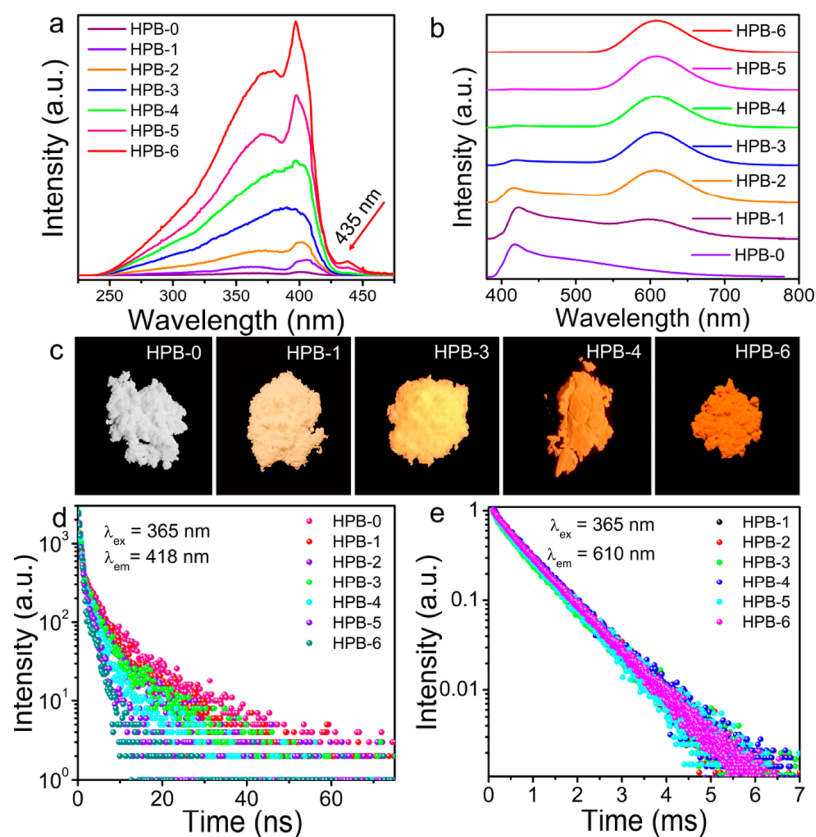


**Figure 2.** Room-temperature absorption and emission spectra excited by 365 nm UV irradiation of $(C_8H_{20}N_2)PbBr_4$ sample.

The absorption spectrum shows a typical excitonic band featured at 385 nm, giving the characteristic absorption peak of layered perovskites.[37] Under the excitation at 365 nm, $(C_8H_{20}N_2)PbBr_4$ gives a broad-band emission, including a narrow peak located at 418 nm and a broad band from 450 to 750 nm, centered at 540 nm. We attribute the dominated narrow band at 418 nm to the FE emission, whereas the weak broad-band emission peaking at 540 nm is considered to be the STE emission. As also confirmed by the distortion calculation, the STE emission is related to the strong electron−phonon coupling in the deformable lattice.[38] Moreover, the relationship between the power density and the emission intensity of the lower-energy broad band further verified that the STEs are the origin of broad band (Figure S2). As is known to all, the Stokes shift of STEs is dependent on the extent of the distortion of the inorganic halide polyhedron. The large Stokes shift of 0.83 eV for $(C_8H_{20}N_2)PbBr_4$ is, in return, verified by the distortion of the $PbBr_6$ polyhedra, as previously discussed.[39]

$Mn^{2+}$-doped 2D perovskites with various doping concentrations are determined as HPB-*x*, where *x* = 0, 1, 2, 3, 4, 5, and 6, corresponding to the nominal $Mn^{2+}$ contents of 0, 0.05, 0.1, 0.2, 0.4, 0.6, and 0.8, respectively, as the $Mn^{2+}/Pb^{2+}$ ratios.
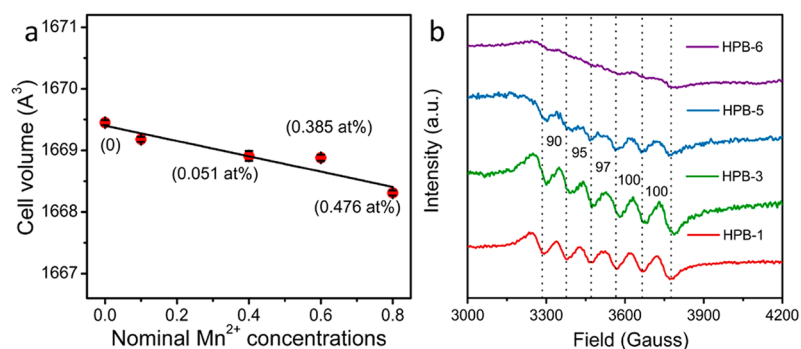
**Figure 3.** (a) Dependence of unit-cell volumes of $(C_8H_{20}N_2)PbBr_4:Mn^{2+}$ on nominal $Mn^{2+}$ concentrations. The actual concentrations are also marked accordingly. (b) Room-temperature X-band EPR spectra of $(C_8H_{20}N_2)PbBr_4:Mn^{2+}$ with different $Mn^{2+}$ concentrations corresponding to HPB-1, HPB-3, HPB-5, and HPB-6 samples.



**Figure 4.** Room-temperature photoluminescence excitation and emission spectra of different $(C_8H_{20}N_2)PbBr_4:Mn^{2+}$ samples with the monitoring wavelength for the (a) excitation ($\lambda_{em}$ = 610 nm) and (b) emission ($\lambda_{ex}$ = 365 nm). (c) Optical photographs of $(C_8H_{20}N_2)PbBr_4:Mn^{2+}$ samples under UV irradiation. Time-resolved PL decay curves of (d) FE emission and (e) $Mn^{2+}$ emission under 365 nm irradiation.

XRD patterns of $Mn^{2+}$-doped $(C_8H_{20}N_2)PbBr_4$ powders are shown in Figure S3. The diffraction patterns of $(C_8H_{20}N_2)$-$PbBr_4:Mn^{2+}$ match well with the pure $(C_8H_{20}N_2)PbBr_4$ phase, and there are no other impurities with increasing $Mn^{2+}$ content. In addition, one can observe that there is little variation for the diffraction peak positions when the nominal added $Mn^{2+}$ content increased. Rietveld refinement of this series of samples is described in Figure S4, and the variation of cell parameters is given in Table S4. On the basis of the detailed structural analysis, the cell volumes of $Mn^{2+}$-doped samples just decrease a little with the increase in $Mn^{2+}$ dopant concentration (Figure 3a). To further prove that $Mn^{2+}$ dopants have been successfully incorporated into the $(C_8H_{20}N_2)PbBr_4$ host, the X-band electron paramagnetic resonance (EPR)

spectra of $Mn^{2+}$-doped samples were measured and are shown in Figure 3b. The EPR spectra of $Mn^{2+}$ ions in the $(C_8H_{20}N_2)PbBr_4$ host contain several lines stemming from the electron and nuclear spin states ($S$ = 5/2, $I$ = 5/2). Therefore, zero field splitting (ZFS) and hyperfine interactions appear due to the point symmetry of $Mn^{2+}$. As shown in Figure 3b, the hyperfine coupling splitting for HPB-1, HPB-3, HPB-5, and HPB-6 samples is observed. The average splitting energy of ~96.4 G is similar to that found in $L_2PbX_4:Mn^{2+}$ (X = Cl, Br, I),[29] which indicated that the $Mn^{2+}$ ion was present in the +2 oxidation state and occupied the octahedral coordination environment of the $Pb^{2+}$ ion with a homogeneous distribution. It further implied the weak $Mn^{2+}-Mn^{2+}$ exchange interaction; therefore, a strong $Mn^{2+}$ emission was observed with high

**Table 1. Nominal and Actual Mn$^{2+}$ Doping Contents and PLQYs in Some Selected Mn$^{2+}$-Doped 2D Halide Perovskites**

| Mn$^{2+}$-doped samples | nominal Mn$^{2+}$ doping contents (Mn$^{2+}$/Pb$^{2+}$) (%) | actual Mn$^{2+}$ contents by ICP (atomic %) | actual Mn$^{2+}$ contents by EDS (atomic %) | PLQY/100% (%) | ref |
|---|---|---|---|---|---|
| Mn$^{2+}$:(But)$_2$PbBr$_4$ | 5 | 1.1 | 0.25 | 37 | 18 |
| Mn$^{2+}$:(BA/OA)$_2$PbBr$_4$ | 10 | 1.1 | 1.74 | 36 | 27 |
| Mn$^{2+}$:Cs$_2$PbCl$_2$I$_2$ | 100 | | 1.7 | 16 | 28 |
| Mn$^{2+}$:(L)$_2$PbBr$_4$ | 100 | 4.2 | | 61 | 29 |
| Mn$^{2+}$:(BA)$_2$PbBr$_4$ | 1000 | 1.08 | | 26 | 30 |
| Mn$^{2+}$:(C$_6$H$_{18}$N$_2$O$_2$)$_2$PbBr$_4$ | 10 | | | 12.54 | 31 |
| Mn$^{2+}$:(C$_4$H$_9$NH$_3$)$_2$PbCl$_4$ | 20 | | 0.18 | 27.9 | 33 |
| Mn$^{2+}$:(BA)$_2$PbBr$_4$ | 20 | | | 60.1 | 36 |
| Mn$^{2+}$:EA$_2$PbBr$_4$ | 40 | | 5 | 78 | 44 |
| Mn$^{2+}$:(C$_8$H$_{20}$N$_2$)PbBr$_4$ | 80 | 0.476 | | 60.8 | this work |

PLQYs; the details will be discussed later. When the nominal Mn$^{2+}$ doping concentration reaches 0.8 (HPB-6) as the ratio of Mn$^{2+}$/Pb$^{2+}$, the EPR spectra exhibit a broadening line because of the heterogeneous distribution of Mn$^{2+}$ caused by the Mn$^{2+}$−Mn$^{2+}$ dipolar and exchange interaction. In consideration of the ratio of Pb$^{2+}$/Mn$^{2+}$ in doped samples, the actual Mn$^{2+}$ contents were surveyed using the inductively coupled plasma optical emission spectroscopy (ICP-OES) technique, which showed that the actual Mn$^{2+}$ contents are only 0.006, 0.019, 0.051, 0.385, and 0.476 at % for HPB-$x$ ($x$ = 1, 3, 4, 5, 6) samples, respectively (Table S5). This result indicated that a trace of Mn$^{2+}$ can be effectively doped into the (C$_8$H$_{20}$N$_2$)-PbBr$_4$ host compared with the nominal content, which is consistent with the minor variation of cell volume shown in Figure 3a.

The photoluminescence excitation (PLE) spectra of Mn$^{2+}$-doped (C$_8$H$_{20}$N$_2$)PbBr$_4$ samples with different Mn$^{2+}$ contents are described in Figure 4a. All of them present a similar sharp exciton characteristic peaking at 396 nm, which stems from the host excitonic absorption. Interestingly, additional characteristic peaks of 435 nm appeared in Mn$^{2+}$-doped samples, also presenting a positive correlation with the concentration of Mn$^{2+}$ ion. This indicates that an absorption peak does not originate exclusively from the host in doped systems, and a midgap state synchronously appears depending on the Mn$^{2+}$ doping. The much lower intensity of midgap states suggests that the energy of Mn$^{2+}$ emission is primarily ascribed to the host absorption. The absorption spectra of the Mn$^{2+}$-doped samples also act as powerful evidence to prove the existence of intermediate trap states due to an additional broad band peak compared with undoped sample (Figure S5).

A broad-band orange-red emission with a peak at 610 nm is found for Mn$^{2+}$-doped (C$_8$H$_{20}$N$_2$)PbBr$_4$ samples, which is ascribed to the $^4T_1$−$^6A_1$ transition of Mn$^{2+}$ (Figure 4b). The emission intensities of STEs and FE peaks gradually decreased depending on increasing Mn$^{2+}$ concentrations. When the actual Mn$^{2+}$ dopant concentration was 0.476 at % (HPB-6), the STEs and FE emission almost completely disappeared. Comparatively, the Mn$^{2+}$ emission kept increasing. Figure 4c shows the photographs of Mn$^{2+}$-doped (C$_8$H$_{20}$N$_2$)PbBr$_4$ samples with different Mn$^{2+}$ contents under UV irradiation, and we can observe the appearance of orange-red emission and the significant enhancement of Mn$^{2+}$ emission with increased Mn$^{2+}$ concentrations. In general, energy transfer from FE excited states to Mn$^{2+}$ d states usually occurs in several hundreds of picoseconds,[40,41] whereas the lattice captures FEs to form STEs on the picosecond time scale in 2D halide perovskites.[42] Therefore, the facts regarding the relatively

slower energy transfer time from FE excited states to Mn$^{2+}$ d states and the faster formation of STE emission indicate that the doping of Mn$^{2+}$ makes no obvious difference for the STEs. However, the observed strong Mn$^{2+}$ emission in this system suggests that the midgap states have been introduced synchronously upon Mn$^{2+}$ doping. In general, dopants lead to the formation of defect states, which, in turn, trap the excitons on the several tens of picoseconds time scale.[43] As a result of exciton trapping, the midgap states, also called trap states, become more competitive than the appearance of STEs.

Because there exist the coupled states comprising Mn$^{2+}$ d states, self-trapped excited states, and FE excited states in (C$_8$H$_{20}$N$_2$)PbBr$_4$:Mn$^{2+}$, the time-resolved luminescence was measured to analyze the excited-state dynamics. The decay curves monitored at two different emission peaks at 418 and 610 nm for FE emissions and Mn$^{2+}$ emission are described in Figure 4c,d, respectively. All emission decay curves monitored at 418 nm demonstrate a similar double-exponential fit, and the average lifetime values decrease from 4.64 to 0.74 ns depending on the increasing Mn$^{2+}$ nominal concentration from 0 to 0.8. More importantly, one can find this significant decline to demonstrate the efficient exciton trapping by defect states.[44] Therefore, more energy can be transferred to the Mn$^{2+}$ ion, leading to efficient Mn$^{2+}$ emission. The luminescence decay curves of STEs are described in Figure S6, which are attributed to the dominated self-trapped excited states and the FE excited states.[45] The lifetime value of STE emission for (C$_8$H$_{20}$N$_2$)-PbBr$_4$ is determined to be 11.71 ns. Because the higher doping concentration leads to a high density of defect states and helps the nonradiative relaxation process, the lifetime values of STEs gradually decreased with increasing Mn$^{2+}$ concentration.[45] In addition, the higher doping concentrations lead to the efficient exciton trapping by defects, also resulting in efficient Mn$^{2+}$ emission. The decay curves of Mn$^{2+}$ emission at 610 nm are illustrated in Figure 4d. The as-measured lifetimes for the emissions of different HPB-$x$ ($x$ = 1, 2, 3, 4, 5, 6) samples were calculated to be nearly identical at ∼0.77 ms, suggesting a typical $^4T_1$ → $^6A_1$ transition of Mn$^{2+}$, as reported in other Mn$^{2+}$-doped halide perovskites.[18] The nearly identical lifetimes of different Mn$^{2+}$-doped samples indicated that there are weak Mn$^{2+}$−Mn$^{2+}$ dipolar and exchange interactions, which can be negligible.

The PLQYs of HPB-0, HPB-1, HPB-2, HPB-3, HPB-4, HPB-5, and HPB-6 are measured to be 6.6, 7.74, 11.19, 13.60, 28.51, 56.00, and 60.80%, respectively (Figure S7). We compared the nominal and actual Mn$^{2+}$ doping contents and PLQYs in some selected Mn$^{2+}$-doped 2D metal halide perovskites (Table 1). On the basis of the data shown in
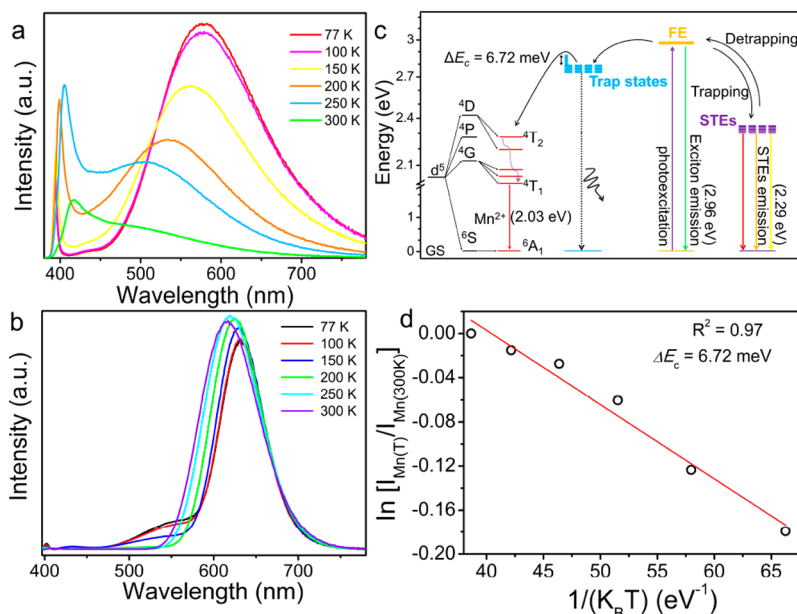
**Figure 5.** Temperature-dependent emission spectra of (a) $(C_8H_{20}N_2)PbBr_4$ and (b) $(C_8H_{20}N_2)PbBr_4:Mn^{2+}$ samples. (c) Schematic diagram of the luminescence mechanism of $(C_8H_{20}N_2)PbBr_4$ and $(C_8H_{20}N_2)PbBr_4:Mn^{2+}$. (d) Boltzmann analysis of the integral intensities of $Mn^{2+}$ emission in $(C_8H_{20}N_2)PbBr_4$:0.476 at % $Mn^{2+}$ (HPB-6).

Table 1, to achieve higher PLQYs, more $Mn^{2+}$ precursor (nominal composition defined by $Mn^{2+}/Pb^{2+}$ ratio) is required, especially for $Mn^{2+}$-doped $(BA)_2PbBr_4$. When the $Pb^{2+}/Mn^{2+}$ ratio increases to 1:10, the PLQY of $(BA)_2PbBr_4:Mn^{2+}$ reaches only 26%. In our work, upon doping 80% $Mn^{2+}$ precursor into $(C_8H_{20}N_2)PbBr_4$, the PLQY can reach 60.8%. As previously mentioned, the chemical compositions measured by the ICP-OES method demonstrated that the actual $Mn^{2+}$ content is only 0.476 at%, which is the smallest $Mn^{2+}$ concentration in Table 1 for achieving a high PLQY of 60.8%. Moreover, the EPR spectra of corresponding samples exhibit homogeneous hyperfine coupling splitting, implying the weak $Mn^{2+}-Mn^{2+}$ exchange interaction. This is because the strong $Mn^{2+}-Mn^{2+}$ exchange interaction will provide an extra pathway for nonradiative energy transfer and result in concentration quenching, which is consistent with the observed photoluminescence phenomenon. At first, when the actual $Mn^{2+}$ concentration increased from 0.006 to 0.385 at %, the PLQY of the corresponding samples dramatically increased to 56% because the existence of $Mn^{2+}$ provides an efficient radiative recombination pathway from the $^4T_1$ excitation state to the $^6A_1$ ground state. With further increased $Mn^{2+}$ concentration up to 0.476 at %, the corresponding PLQY slowly increased to 60.8% due to the nonradiative energy transfer caused by the increased $Mn^{2+}-Mn^{2+}$ dipolar and exchange interactions, which is conformed by the observed by EPR spectra and the nearly identical lifetimes. As a further consideration, the observed weak $Mn^{2+}-Mn^{2+}$ dipolar and exchange interactions in this work are ascribed to the large $Mn^{2+}-Mn^{2+}$ distance caused by the large organic molecule, with the interlayer distance of the inorganic layer up to 12.22 Å, and thus efficient $Mn^{2+}$ emission was realized in low-$Mn^{2+}$-concentration-doped $(C_8H_{20}N_2)$-$PbBr_4$. As a result, compared with other $Mn^{2+}$-doped hybrid perovskites, $Mn^{2+}$-doped $(C_8H_{20}N_2)PbBr_4$ shows a greater advantage in highly efficient photoluminescence for further applications.

Therefore, the involved mechanism of efficient $Mn^{2+}$ emission here is a challenge and deserves to be studied. As is well known, there is an obvious difference in excited state dynamics between the $Mn^{2+}$-doped 3D and 2D halide perovskites. For the former, the energy transfer from the FE excited states to the $Mn^{2+}$ d states is due to a two-step sensitization process, in which intermediate trap states assist this energy transfer process.[46,47] Furthermore, $Mn^{2+}$ emission can capture the energy entirely from nonradiative trap states instead of from band states.[48] For the latter, $Mn^{2+}$ emission usually stems from the energy transfer from the FE excited states to the $Mn^{2+}$ d states.[18] Recently, Luo et al. also found that efficient energy transfer from the FE excited states to $Mn^{2+}$ d states is assisted by intermediate trap states in $Mn^{2+}$-doped 2D $(EA)_2PbBr_4$ with STE emission.[44] This is because the STEs belong to a kind of indirect transient state without a ground energy level, which will prevent the electron exchange in Dexter energy transfer,[45,49] and thus one cannot find the energy transfer from self-trapped excited states to $Mn^{2+}$ d states. In our case, we observed that the energy of $Mn^{2+}$ is not completely provided by the FE, and the energy transfer from FE excited states to $Mn^{2+}$ d states happens due to intermediate trap states. Thus to further investigate the photoluminescence mechanism of the present $Mn^{2+}$-doped $(C_8H_{20}N_2)PbBr_4$ system, we comparatively studied the temperature-dependent PL spectra of $(C_8H_{20}N_2)PbBr_4$ and $(C_8H_{20}N_2)PbBr_4:Mn^{2+}$ (Figure 5a,b). At low temperature, two emission peaks deriving from FE and STEs are found for both of them. With increasing temperature, the FE and STE emissions decrease, whereas the d−d transition of the $Mn^{2+}$ ion for the doped samples is gradually enhanced. Therefore, the schematic energy level diagram is described in Figure 5c, demonstrating the coupled FE, STE, trap, and $Mn^{2+}$ d states in the $(C_8H_{20}N_2)PbBr_4:Mn^{2+}$ system. Under excitation by UV light at low temperature, FEs are generated and trapped by the self-trapped excited states. Along with increasing temperature, the detrapping of excitons is thermally activated, which causes increasing FE emission and

decreasing STEs emission. The increased FE emission leads to the efficient trapping of excitons, as previously discussed; then, the energy transfer rate of the trap states to $Mn^{2+}$ d states increases with the enhancement of the $Mn^{2+}$ emission. In addition, there is a competition between the FE recombination and the energy transfer from FE excited states to $Mn^{2+}$ d states. With increasing $Mn^{2+}$ concentrations, on the one hand, the higher doping concentration results in the efficient trapping of excitons by defects, resulting in efficient $Mn^{2+}$ emission. On the other hand, the existence of $Mn^{2+}$ provides an efficient radiative recombination pathway from $^4T_1$ excitation state to the $^6A_1$ ground state, leading to increased $Mn^{2+}$ emission. Therefore, PLQYs demonstrate a tendency to increase with increasing $Mn^{2+}$ concentration. It is worth noting that with the temperature increase from 250 to 300 K, the gradual decrease in the $Mn^{2+}$ emission demonstrates the thermally activated excitation mechanism of dopants. In this case, one can calculate the activation energy $\Delta E_c$ based on the Boltzmann analysis shown in Figure 5d. Thus the calculated $\Delta E_c$ is determined to be 6.72 meV, which is much smaller than that in $CsPbCl_3$ nanocrystals ($\sim$314 meV).[46] This small potential barrier is also the reason for realizing efficient energy transfer from FE excited states to $Mn^{2+}$ d states at room temperature.

In summary, we designed and prepared the novel $Mn^{2+}$-doped 2D halide perovskite $(C_8H_{20}N_2)PbBr_4$, and a strong orange-red emission peaking at 610 nm was observed originating from the $^4T_1 \rightarrow {}^6A_1$ transition of $Mn^{2+}$. The actual $Mn^{2+}$ doping content is determined to be 0.476 at % with a high PLQY of up to 60.8%. The excited state dynamics and photoluminescence mechanism herein involved the interaction and energy transfer in coupled states, including $Mn^{2+}$ d states, FE excited states, self-trapped excited states, and trap states. The efficient trapping of excitons by defects and the small activation energy ($\sim$6.72 meV) promote the energy transfer between the trap states and the $Mn^{2+}$ d states, suggesting the highly efficient orange-red emission in $Mn^{2+}$-doped 2D halide perovskite. Moreover, $Mn^{2+}$–$Mn^{2+}$ dipolar and exchange interactions make a small difference in the photoluminescence properties. This work provides new ideas on how understanding the doping amount and energy states of $Mn^{2+}$ activators in the halide perovskites enables us to control the efficient energy transfer and photoluminescence for light-emitting diode applications.

## ASSOCIATED CONTENT

### Ⓢ Supporting Information

The Supporting Information is available free of charge at https://pubs.acs.org/doi/10.1021/acs.jpclett.0c00593.

Figures S1–S7. Photoluminescence properties of the studied materials. Tables S1–S5. Main parameters of processing and refinement, fractional atomic coordinates and isotropic displacement parameters, and main geometric parameters (PDF)

Crystallographic information on $(C_8H_{20}N_2)PbBr_4$ (CIF)

## AUTHOR INFORMATION

### Corresponding Author

**Zhiguo Xia** − The State Key Laboratory of Luminescent Materials and Devices, Guangdong Provincial Key Laboratory of Fiber Laser Materials and Applied Techniques, School of Materials Science and Technology, South China University of Technology, Guangzhou 510640, P. R. China; orcid.org/0000-0002-9670-3223; Email: xiazg@scut.edu.cn

### Authors

**Binbin Su** − The State Key Laboratory of Luminescent Materials and Devices, Guangdong Provincial Key Laboratory of Fiber Laser Materials and Applied Techniques, School of Materials Science and Technology, South China University of Technology, Guangzhou 510640, P. R. China

**Maxim S. Molokeev** − Laboratory of Crystal Physics, Kirensky Institute of Physics, Federal Research Center KSC SB RAS, Krasnoyarsk 660036, Russia; Siberian Federal University, Krasnoyarsk 660041, Russia; Department of Physics, Far Eastern State Transport University, Khabarovsk 680021, Russia

Complete contact information is available at:
https://pubs.acs.org/10.1021/acs.jpclett.0c00593

### Notes

The authors declare no competing financial interest.

## REFERENCES

(1) Saparov, B.; Mitzi, D. B. Organic−Inorganic Perovskites: Structural Versatility for Functional Materials Design. *Chem. Rev.* **2016**, *116*, 4558−4596.

(2) Quan, L. N.; Rand, B. P.; Friend, R. H.; Mhaisalkar, S. G.; Lee, T. W.; Sargent, E. H. Perovskites for Next-Generation Optical Sources. *Chem. Rev.* **2019**, *119*, 7444−7477.

(3) Erwin, S. C.; Zu, L.; Haftel, M. I.; Efros, A. L.; Kennedy, T. A.; Norris, D. J. Doping Semiconductor Nanocrystals. *Nature* **2005**, *436*, 91−4.

(4) Zhou, Y.; Chen, J.; Bakr, O. M.; Sun, H. T. Metal-Doped Lead Halide Perovskites: Synthesis, Properties, and Optoelectronic Applications. *Chem. Mater.* **2018**, *30*, 6589−6613.

(5) Li, S.; Shi, Z. F.; Zhang, F.; Wang, L. T.; Ma, Z. Z.; Yang, D. W.; Yao, Z. Q.; Wu, D.; Xu, T. T.; Tian, Y. T.; Zhang, Y. T.; Shan, C. X.; Li, X. J. Sodium Doping-Enhanced Emission Efficiency and Stability of CsPbBr$_3$ Nanocrystals for White Light-Emitting Devices. *Chem. Mater.* **2019**, *31*, 3917−3928.

(6) Bi, C. H.; Wang, S. X.; Li, Q.; Kershaw, S. V.; Tian, J. J.; Rogach, A. L. Thermally Stable Copper (II)-Doped Cesium Lead Halide Perovskite Quantum Dots with Strong Blue Emission. *J. Phys. Chem. Lett.* **2019**, *10*, 943−952.

(7) Shen, X. Y.; Zhang, Y.; Kershaw, S. V.; Li, T.; Wang, C. C.; Zhang, X. Y.; Wang, W. Y.; Li, D. G.; Wang, Y. H.; Lu, M.; et al. Zn-Alloyed CsPbI$_3$ Nanocrystals for Highly Efficient Perovskite Light-Emitting Devices. *Nano Lett.* **2019**, *19*, 1552−1559.

(8) Cai, T.; Yang, H. J.; Hills-Kimball, K.; Song, J.-P.; Zhu, H.; Hofman, E.; Zheng, W.; Rubenstein, B. M.; Chen, O. Synthesis of All-inorganic Cd-Doped CsPbCl$_3$ Perovskite Nanocrystals with Dual-Wavelength Emission. *J. Phys. Chem. Lett.* **2018**, *9*, 7079−7084.

(9) Lu, M.; Zhang, X. Y.; Zhang, Y.; Guo, J.; Shen, X. Y.; Yu, W. W.; Rogach, A. L. Simultaneous Strontium Doping and Chlorine Surface Passivation Improve Luminescence Intensity and Stability of CsPbI$_3$

Nanocrystals Enabling Efficient Light-Emitting Devices. *Adv. Mater.* **2018**, *30*, 1804691.

(10) Liu, W.; Lin, Q.; Li, H.; Wu, K.; Robel, I.; Pietryga, J. M.; Klimov, V. I. Mn$^{2+}$-Doped Lead Halide Perovskite Nanocrystals with Dual-Color Emission Controlled by Halide Content. *J. Am. Chem. Soc.* **2016**, *138*, 14954.

(11) Nag, A.; Chakraborty, S.; Sarma, D. D. To Dope Mn$^{2+}$ in a Semiconducting Nanocrystal. *J. Am. Chem. Soc.* **2008**, *130*, 10605−11.

(12) Guria, A. K.; Dutta, S. K.; Adhikari, S. D.; Pradhan, N. Doping Mn$^{2+}$ in Lead Halide Perovskite Nanocrystals: Successes and Challenges. *ACS Energy Lett.* **2017**, *2*, 1014−1021.

(13) Du, P.; Luo, L. H.; Cheng, W. Neoteric Mn$^{2+}$-Activated Cs$_3$Cu$_2$I$_5$ Dazzling Yellow-Emitting Halides Towards White-LED. *J. Am. Ceram. Soc.* **2020**, *103*, 1149−1155.

(14) Nayak, P. K.; Sendner, M.; Wenger, B.; Wang, Z.; Sharma, K.; Ramadan, A. J.; Lovrinčić, R.; Pucci, A.; Madhu, P. K.; Snaith, H. J. Impact of Bi$^{3+}$ Heterovalent Doping in Organic-Inorganic Metal Halide Perovskite Crystals. *J. Am. Chem. Soc.* **2018**, *140*, 574−577.

(15) Gangishetty, M. K.; Sanders, S. N.; Congreve, D. N. Mn$^{2+}$ Doping Enhances the Brightness, Efficiency, and Stability of Bulk Perovskite Light-Emitting Diodes. *ACS Photonics* **2019**, *6*, 1111−1117.

(16) Mir, W. J.; Jagadeeswararao, M.; Das, S.; Nag, A. Colloidal Mn-Doped Cesium Lead Halide Perovskite Nanoplatelets. *ACS Energy Lett.* **2017**, *2*, 537−543.

(17) Parobek, D.; Roman, B. J.; Dong, Y.; Jin, H.; Lee, E.; Sheldon, M.; Son, D. H. Exciton-to-Dopant Energy Transfer in Mn-Doped Cesium Lead Halide Perovskite Nanocrystals. *Nano Lett.* **2016**, *16*, 7376−7380.

(18) Biswas, A.; Bakthavatsalam, R.; Kundu, J. Efficient Exciton to Dopant Energy Transfer in Mn$^{2+}$-Doped (C$_4$H$_9$NH$_3$)$_2$PbBr$_4$ Two-Dimensional (2D) Layered Perovskites. *Chem. Mater.* **2017**, *29*, 7816−7825.

(19) Arunkumar, P.; Cho, H. B.; Gil, K. H.; Unithrattil, S.; Kim, Y. H.; Bin Im, W. Probing Molecule-Like Isolated Octahedra via-Phase Stabilization of Zero-Dimensional Cesium Lead Halide Nanocrystals. *Nat. Commun.* **2018**, *9*, 4691.

(20) Zhou, J.; Rong, X. M.; Zhang, P.; Molokeev, M. S.; Wei, P. J.; Liu, Q. L.; Zhang, X. W.; Xia, Z. G. Manipulation of Bi$^{3+}$/In$^{3+}$ Transmutation and Mn$^{2+}$-Doping Effect on the Structure and Optical Properties of Double Perovskite Cs$_2$NaBi$_{1-x}$In$_x$Cl$_6$. *Adv. Opt. Mater.* **2019**, *7*, 1801435.

(21) Smith, M. D.; Connor, B. A.; Karunadasa, H. I. Tuning the Luminescence of Layered Halide Perovskites. *Chem. Rev.* **2019**, *119*, 3104−3139.

(22) Zhang, L.; Liu, Y.; Yang, Z.; Liu, S. Two Dimensional Metal Halide Perovskites: Promising Candidates for Light-Emitting Diodes. *J. Energy Chem.* **2019**, *37*, 97−110.

(23) Tan, Z. J.; Wu, Y.; Hong, H.; Yin, J. B.; Zhang, J.; Lin, L.; Wang, M. Z.; Sun, X.; Sun, L. Z.; Huang, Y. C.; Liu, K. H.; Liu, Z. F.; Peng, H. L. Two-Dimensional (C4H$_9$NH$_3$)$_2$PbBr$_4$ Perovskite Crystals for High-Performance Photodetector. *J. Am. Chem. Soc.* **2016**, *138*, 16612−16615.

(24) Shi, E. Z.; Gao, Y.; Finkenauer, B. P.; Akriti; Coffey, A. H.; Dou, L. T. Two-Dimensional Halide Perovskite Nanomaterials and Heterostructures. *Chem. Soc. Rev.* **2018**, *47*, 6046−6072.

(25) Mao, L. L.; Stoumpos, C. C.; Kanatzidis, M. G. Two-Dimensional Hybrid Halide Perovskites: Principles and Promises. *J. Am. Chem. Soc.* **2019**, *141*, 1171−1190.

(26) Hu, J.; Yan, L.; You, W. Two-Dimensional Organic-Inorganic Hybrid Perovskites: A New Platform for Optoelectronic Applications. *Adv. Mater.* **2018**, *30*, 1802041.

(27) Usman, M. H. P.; Bakthavatsalam, R.; Kundu, J. Colloidal Mn$^{2+}$ Doped 2D (n = 1) Lead Bromide Perovskites: Efficient Energy Transfer and Role of Anion in Doping Mechanism. *ChemistrySelect* **2018**, *3*, 6585−6595.

(28) Dutta, A.; Behera, R. K.; Deb, S.; Baitalik, S.; Pradhan, N. Doping Mn(II) in All-Inorganic Ruddlesden-Popper Phase of Tetragonal Cs$_2$PbCl$_2$I$_2$ Perovskite Nanoplatelets. *J. Phys. Chem. Lett.* **2019**, *10*, 1954−1959.

(29) Dutta, S. K.; Dutta, A.; Das Adhikari, S.; Pradhan, N. Doping Mn$^{2+}$ in Single-Crystalline Layered Perovskite Microcrystals. *ACS Energy Lett.* **2019**, *4*, 343−351.

(30) Sheikh, T.; Nag, A. Mn Doping in Centimeter-Sized Layered 2D Butylammonium Lead Bromide (BA$_2$PbBr$_4$) Single Crystals and Their Optical Properties. *J. Phys. Chem. C* **2019**, *123*, 9420−9427.

(31) Zhou, G. J.; Jiang, X. X.; Molokeev, M. S.; Lin, Z. S.; Zhao, J.; Wang, J.; Xia, Z. G. Optically Modulated Ultra-Broad-Band Warm White Emission in Mn$^{2+}$-Doped (C$_6$H$_{18}$N$_2$O$_2$)PbBr$_4$ Hybrid Metal Halide Phosphor. *Chem. Mater.* **2019**, *31*, 5788−5795.

(32) Bakthavatsalam, R.; Biswas, A.; Chakali, M.; Bangal, P. R.; Kore, B. P.; Kundu, J. Temperature-Dependent Photoluminescence and Energy-Transfer Dynamics in Mn$^{2+}$-Doped (C$_4$H$_9$NH$_3$)$_2$PbBr$_4$ Two-Dimensional (2D) Layered Perovskite. *J. Phys. Chem. C* **2019**, *123*, 4739−4748.

(33) Zhou, G. J.; Guo, S. Q.; Zhao, J.; Molokeev, M.; Liu, Q. L.; Zhang, J. Y.; Xia, Z. G. Unraveling the Mechanochemical Synthesis and Luminescence in Mn$^{II}$-Based Two-Dimensional Hybrid Perovskite (C$_4$H$_9$NH$_3$)$_2$PbCl$_4$. *Sci. China Mater.* **2019**, *62*, 1013−1022.

(34) van der Stam, W.; Geuchies, J. J.; Altantzis, T.; van den Bos, K. H. W.; Meeldijk, J. D.; Van Aert, S.; Bals, S.; Vanmaekelbergh, D.; de Mello Donega, C. Highly Emissive Divalent-Ion-Doped Colloidal CsPb$_{1-x}$M$_x$Br$_3$ Perovskite Nanocrystals through Cation Exchange. *J. Am. Chem. Soc.* **2017**, *139*, 4087−4097.

(35) Swarnkar, A.; Ravi, V. K.; Nag, A. Beyond Colloidal Cesium Lead Halide Perovskite Nanocrystals: Analogous Metal Halides and Doping. *ACS Energy Lett.* **2017**, *2*, 1089−1098.

(36) Zhou, G. J.; Jia, X. F.; Guo, S. Q.; Molokeev, M. S.; Zhang, J. Y.; Xia, Z. G. Role of Halogen Atoms on High-Efficiency Mn$^{2+}$ Emission in Two-Dimensional Hybrid Perovskites. *J. Phys. Chem. Lett.* **2019**, *10*, 4706−4712.

(37) Neogi, I.; Bruno, A.; Bahulayan, D.; Goh, T. W.; Ghosh, B.; Ganguly, R.; Cortecchia, D.; Sum, T. C.; Soci, C.; Mathews, N.; Mhaisalkar, S. G. Broadband-Emitting 2D Hybrid Organic-Inorganic Perovskite Based on Cyclohexane-bis(methylamonium) Cation. *ChemSusChem* **2017**, *10*, 3765−3772.

(38) Cortecchia, D.; Neutzner, S.; Srimath Kandada, A. R.; Mosconi, E.; Meggiolaro, D.; De Angelis, F.; Soci, C.; Petrozza, A. Broadband Emission in Two-Dimensional Hybrid Perovskites: The Role of Structural Deformation. *J. Am. Chem. Soc.* **2017**, *139*, 39−42.

(39) Wang, S. S.; Yao, Y. P.; Kong, J. T.; Zhao, S. G.; Sun, Z. H.; Wu, Z. Y.; Li, L. N.; Luo, J. H. Highly Efficient White-Light Emission in a Polar Two-Dimensional Hybrid Perovskite. *Chem. Commun.* **2018**, *54*, 4053−4056.

(40) De, A.; Mondal, N.; Samanta, A. Luminescence Tuning and Exciton Dynamics of Mn-Doped CsPbCl$_3$ Nanocrystals. *Nanoscale* **2017**, *9*, 16722−16727.

(41) Rossi, D.; Parobek, D.; Dong, Y. T.; Son, D. H. Dynamics of Exciton-Mn Energy Transfer in Mn-Doped CsPbCl$_3$ Perovskite Nanocrystals. *J. Phys. Chem. C* **2017**, *121*, 17143−17149.

(42) Hu, T.; Smith, M. D.; Dohner, E. R.; Sher, M.-J.; Wu, X.; Trinh, M. T.; Fisher, A.; Corbett, J.; Zhu, X.-Y.; Karunadasa, H. I.; et al. Mechanism for Broadband White-Light Emission From Two-Dimensional (110) Hybrid Perovskites. *J. Phys. Chem. Lett.* **2016**, *7*, 2258−2263.

(43) Luo, B. B.; Pu, Y. C.; Yang, Y.; Lindley, S. A.; Abdelmageed, G.; Ashry, H.; Li, Y.; Li, X. M.; Zhang, J. Z. Synthesis, Optical Properties, and Exciton Dynamics of Organolead Bromide Perovskite Nanocrystals. *J. Phys. Chem. C* **2015**, *119*, 26672−26682.

(44) Luo, B. B.; Guo, Y.; Li, X. L.; Xiao, Y. H.; Huang, X. C.; Zhang, J. Z. Efficiently Trap-Mediated Mn$^{2+}$ Dopant Emission in 2D Single-Layered Perovskite (CH$_3$CH$_2$NH$_3$)$_2$PbBr$_4$. *J. Phys. Chem. C* **2019**, *123*, 14239−14245.

(45) Zhou, C. K.; Tian, Y.; Khabou, O.; Worku, M.; Zhou, Y.; Hurley, J.; Lin, H. R.; Ma, B. W. Manganese-Doped One-Dimensional Organic Lead Bromide Perovskites with Bright White Emissions. *ACS Appl. Mater. Interfaces* **2017**, *9*, 40446−40451.

(46) Pinchetti, V.; Anand, A.; Akkerman, Q. A.; Sciacca, D.; Lorenzon, M.; Meinardi, F.; Fanciulli, M.; Manna, L.; Brovelli, S. Trap-Mediated Two-Step Sensitization of Manganese Dopants in Perovskite Nanocrystals. *ACS Energy Lett.* **2019**, *4*, 85−93.

(47) Forde, A.; Inerbaev, T.; Kilin, D. Spinor Dynamics in Pristine and $Mn^{2+}$-Doped $CsPbBr_3$ NC: Role of Spin-Orbit Coupling in Ground- and Excited-State Dynamics. *J. Phys. Chem. C* **2018**, *122*, 26196−26213.

(48) Wei, Q.; Li, M. J.; Zhang, Z. P.; Guo, J.; Xing, G. C.; Sum, T. C.; Huang, W. Efficient Recycling of Trapped Energies for Dual-Emission in Mn-Doped Perovskite Nanocrystals. *Nano Energy* **2018**, *51*, 704−710.

(49) Yuan, H.; Massuyeau, F.; Gautier, N.; Kama, A. B.; Faulques, E.; Chen, F.; Shen, Q.; Zhang, L.; Paris, M.; Gautier, R. Doped Lead Halide White Phosphors for Very High Efficiency and Ultra High Color Rendering. *Angew. Chem.* **2020**, *132*, 2824−2829.